Editors' Suggestion

Resonant Elastic X-Ray Scattering of Antiferromagnetic Superstructures in $EuPtSi_3$

Wolfgang Simeth,[1,2,*] Andreas Bauer,[1,3] Christian Franz,[1,4] Aisha Aqeel,[1,5] Pablo J. Bereciartua,[6]
Jennifer A. Sears,[6] Sonia Francoual,[6] Christian H. Back,[1,3,5] and Christian Pfleiderer[1,3,5]
[1]*Physik-Department, Technische Universität München, D-85748 Garching, Germany*
[2]*Laboratory for Neutron and Muon Instrumentation, Paul Scherrer Institute, CH-5232 Villigen, Switzerland*
[3]*Zentrum für QuantumEngineering (ZQE), Technische Universität München, D-85748 Garching, Germany*
[4]*Jülich Centre for Neutron Science (JCNS) at Heinz Maier-Leibnitz Zentrum (MLZ), D-85748 Garching, Germany*
[5]*Munich Center for Quantum Science and Technology (MCQST), Technische Universität München, D-85748 Garching, Germany*
[6]*Deutsches Elektronen-Synchrotron (DESY), D-22607 Hamburg, Germany*

(Received 15 November 2022; revised 6 April 2023; accepted 11 May 2023; published 26 June 2023)

We report resonant elastic x-ray scattering of long-range magnetic order in $EuPtSi_3$, combining different scattering geometries with full linear polarization analysis to unambiguously identify magnetic scattering contributions. At low temperatures, $EuPtSi_3$ stabilizes type A antiferromagnetism featuring various long-wavelength modulations. For magnetic fields applied in the hard magnetic basal plane, well-defined regimes of cycloidal, conical, and fanlike superstructures may be distinguished that encompass a pocket of commensurate type A order without superstructure. For magnetic field applied along the easy axis, the phase diagram comprises the cycloidal and conical superstructures only. Highlighting the power of polarized resonant elastic x-ray scattering, our results reveal a combination of magnetic phases that suggest a highly unusual competition between antiferromagnetic exchange interactions with Dzyaloshinsky-Moriya spin-orbit coupling of similar strength.

DOI: 10.1103/PhysRevLett.130.266701

In recent years great efforts have been made to identify magnetic superstructures in bulk materials, thin films, and nanoscaled systems [1–5]. In systems comprising ferromagnetic exchange with Dzyaloshinsky-Moriya (DM) spin-orbit coupling [6,7], major discoveries include long-wavelength incommensurate modulations [8–11], solitonic structures [12], and topologically nontrivial order such as skyrmion lattices [13–19]. While these modulated states under applied magnetic field may feature transitions between different superstructures, they collapse at a well-defined transition into a field-polarized state [20–22]. In comparison, less is known about materials comprising antiferromagnetic exchange with DM interactions, as the mere number of possible modulated structures is much larger. Representing the perhaps most general condition, an unresolved question concerns possible magnetic order in the presence of antiferromagnetic exchange and DM interactions of similar strength.

Focusing on magnetic ions such as Eu^{2+} or Gd^{3+}, in which quenched orbital momentum gives way to almost unconstrained spin degrees of freedom, a rich variety of antiferromagnetic states has attracted great interest. Topical examples include incommensurate antiferromagnetism and a large topological Hall effect in $EuGa_2Al_2$ and $EuAl_4$ [23–28], complex antiferromagnetism in $GdRh_2Si_2$, skyrmion lattice order in $GdRu_2Si_2$ [29,30], Gd_2PdSi_3 [31], and $Gd_3Ru_4Al_{12}$ [32], colossal magnetoresistance in compounds such as EuX_2Y_2 ($X = \mathrm{Cd}$, In and $Y = \mathrm{As}$, Sb, P) [33–43], as well as magnetic order and superconductivity in EuX_2As_2 ($X = \mathrm{Fe}$, Ni, Cr, Co) and related compounds [44–46]. These systems, however, lack global DM interactions in their centrosymmetric crystal structures. This is contrasted by the observation of magnetic superstructures, superconductivity, and quantum criticality in $EuTX_3$, where $T = \mathrm{Pt}$, Pd, Ni, Rh, Co, Ir and $X = \mathrm{Si}$, Ge, Sn, Ga, most of which lack inversion symmetry [47–59].

For our study, we selected $EuPtSi_3$, which crystallizes in the noncentrosymmetric tetragonal $BaNiSn_3$ structure (space group $I4mm$), shown in Fig. 1(a) [60]. Measurements of the bulk properties established the characteristics of antiferromagnetic order of localized Eu^{2+} moments below a transition temperature $T_N = 17$ K [61]. Depending on field direction, up to four different phase pockets, denoted A–D, were identified, as shown in Fig. 1(b) for field parallel $\langle 110 \rangle$. For the point group symmetry of $EuPtSi_3$, DM vectors $\boldsymbol{D}_{ij}$ are permitted that support the formation of superlattice structures with Néel-type twisting including antiferromagnetic Néel skyrmions [5,62]. Preliminary neutron scattering suggested some form of superlattice modulation with a wavelength of about 100 Å at zero field, however, without information on the nature of the underlying antiferromagnetism [61].

Experimentally, the unambiguous determination of complex antiferromagnetic spin structures is especially demanding, requiring scattering techniques with high momentum resolution at large momentum transfers, and the possibility to obtain element-specific information and to separate spin and orbital degrees of freedom. Moreover, in many cases tiny sample volumes are available only, e.g., in the form of thin films, nanoscale systems, or bulk samples of highest purity. While neutron scattering has become indispensable in studies of magnetic structures, it cannot meet these general requirements, not to mention prohibitively strong neutron absorption in elements such as Eu, Gd, or Cd. In contrast, seminal studies of comparatively simple magnetic structures in selected rare-earth compounds have demonstrated the capability of resonant elastic x-ray scattering (REXS) with full linear polarization analysis (FLPA) to overcome these challenges [38,63–66].

Using REXS, we determined the four antiferromagnetically ordered phases of $EuPtSi_3$. As a main result, we find that all antiferromagnetic phases represent variations of the same type A antiferromagnetism, where the tetragonal [001] axis is the easy magnetic direction. Combining different scattering geometries and FLPA, we identify long-wavelength cycloidal, conical, and fanlike superstructures, consistent with the DM vectors expected in space group *I*4*mm* [61]. At intermediate fields, the conical and fanlike superstructures encompass a phase pocket of pure type A antiferromagnetism without superstructure, reflecting antiferromagnetic exchange and DM interactions of similar strength. For field along [001], only the phases with cycloidal and conical superstructures are stabilized.

For the REXS experiments, a polished single-crystal cube with an edge length of 2 mm was used as prepared from an ingot grown by means of the optical floating-zone technique [67,74]. The same sample was also used for the study of the magnetization, ac susceptibility, and specific heat reported in Ref. [61]. REXS was carried out in the second experimental hutch EH2 of beam line P09 at the synchrotron source PETRA III [75]. Hard x rays at an incident photon energy of 7.61 keV were used close to the L_{II} edge of europium, cf. Fig. 1(a), where the magnetic cross section is dominated by electric dipole transitions [76]. The x-ray diffraction was carried out in a horizontal scattering geometry and the polarization of the scattered beam was analyzed using PG006 as the analyzer crystal [67,77], permitting a clean polarization analysis, i.e., with negligible analyzer leakage. Magnetic structure refinement by means of a FLPA was carried out using a double phase retarder [77] in combination with the analyzer. In this setup, the polarization plane of the incident beam was rotated rather than the sample, which permits us to avoid parasitic mixing due to slightly different beam spot positions on the sample as well as differences of angular positions of the

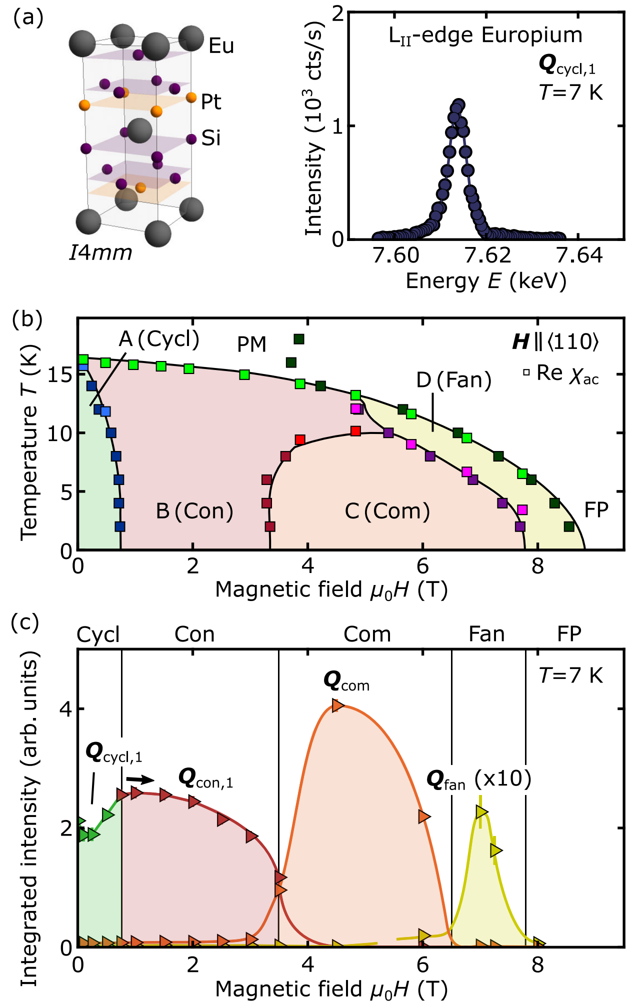

FIG. 1. Crystallographic and magnetic properties of $EuPtSi_3$. (a) Tetragonal unit cell of $EuPtSi_3$, space group *I*4*mm*, and resonant enhancement of the magnetic Bragg intensity when tuning the incident photon energy across the L_{II} edge of europium, characteristic of magnetism predominantly carried by Eu^{2+} moments. (b) Magnetic phase diagram for field parallel to $[\bar{1}10]$, as inferred from susceptibility $\mathrm{Re}\chi_{\mathrm{ac}}$ [61]. Antiferromagnetic phases with cycloidal (Cycl, green), conical (Con, red), commensurate (Com, orange), and fanlike (Fan, yellow) order as well as paramagnetic (PM) and field-polarized (FP) regimes may be distinguished. (c) Field dependence of the REXS intensities at Bragg positions characteristic of the different magnetic phases.

diffractometer. Further information on the sample alignment, the mathematical description of polarized REXS, and the magnetic structure determination may be found in the Supplemental Material [67].

The sample was cooled using a variable temperature insert. A cryomagnet was used to apply vertical magnetic fields of up to 14 T, where two field orientations were studied. In a first experiment, the magnetic field was applied in the tetragonal basal plane enclosing an angle of 20 deg with the $[\bar{1}10]$ axis. This way, the magnetic scattering of all domains could be studied in a single

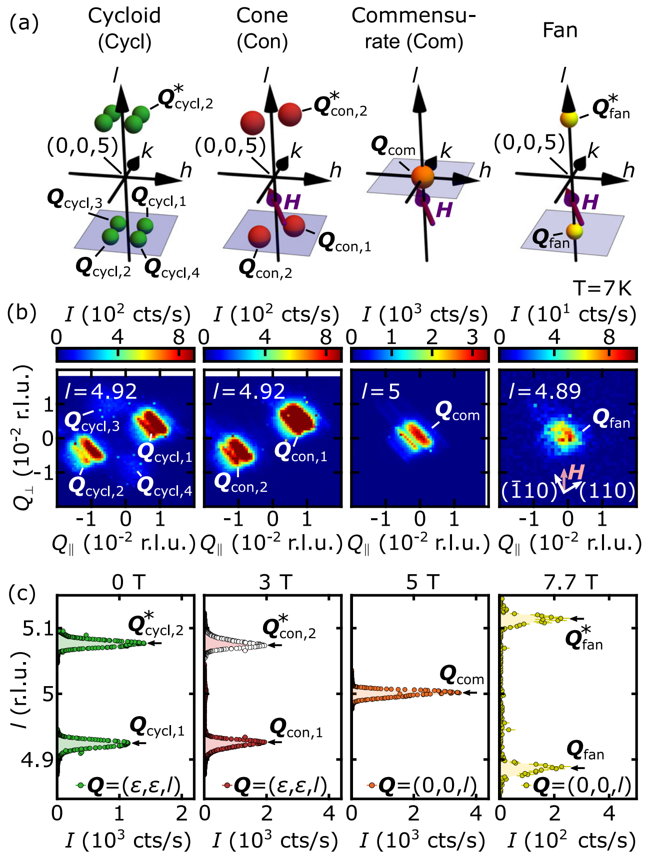

FIG. 2. Resonant elastic x-ray scattering. (a) Schematic depiction of the REXS intensity around the reciprocal-space position $(h,k,l)=(0,0,5)$ in the four ordered phases established in bulk measurements [61]. Maxima at positions $\boldsymbol{Q}$ are indexed with the name of the phase. Arabic numbers indicate crystallographically equivalent positions attributed to different magnetic domains. Positions $\boldsymbol{Q}$ and $\boldsymbol{Q}^*$ are mirrored with respect to (0, 0, 5) and belong to the same domain. Magnetic field $\boldsymbol{H}$ was applied along a nonsymmetry axis within the basal plane in order to discriminate single-domain and multidomain states by means of their evolution under field, cf. Supplemental Material for data with field parallel to $\langle 110\rangle$ [67]. (b) Intensity distributions recorded across planes of constant l, marked by blue shading in (a). (c) Intensity when scanning l through characteristic magnetic Bragg peaks at constant h and k. For clarity, in the conical phase data were mirrored at $l=5$ (open symbols).

scattering channel, namely, $\pi\rightarrow\sigma'$. In a second experiment, the magnetic field was applied parallel to the crystallographic $[\bar{1}10]$ axis, for which the evolution of domain populations as a function of field permitted us to discriminate multi-$\boldsymbol{k}$ from single-$\boldsymbol{k}$ characteristics [61,67]. The FLPA was carried out for this high-symmetry configuration. Data shown in Figs. 1 and 2 were recorded with the first configuration; data shown in Fig. 3 were recorded with the second configuration; further data are shown in the Supplemental Material [67]. For clarity, momentum transfers are given in reciprocal lattice units (r.l.u.), corresponding to $2\pi/a$ along directions h and k or $2\pi/c$ along l.

For all four antiferromagnetic phases, REXS intensity was recorded at specific positions $\boldsymbol{Q}$ in the vicinity of the reciprocal-space position $(h,k,l)=(0,0,5)$, which is crystallographically forbidden. As shown in Fig. 1(c), the integrated scattering intensities as a function of field reflect accurately the phase boundaries of the magnetic phase diagram. The intensity distributions are depicted schematically in the form of colored spheres in Fig. 2(a). Typical REXS data are presented in the form of two-dimensional maps inferred from scans at constant l in Fig. 2(b) and scans along l at fixed h and k in Fig. 2(c). The data presented below were measured under a rotation of the linear polarization by 90 deg, namely, in the $\pi\rightarrow\sigma'$ channel, characteristic of magnetic scattering [76].

In phase A ($H<H_1$), eight magnetic satellites were observed at $(\pm\epsilon,\pm\epsilon,5\pm\delta_1)$ with $\epsilon=0.007(1)$ and $\delta_1=0.077(6)$ (green spheres). This field distribution implies superlattice modulations of the staggered magnetization with $c/(2\delta_1)\approx 64$ Å along [001] and $a/(2\sqrt{2}\epsilon)\approx 215$ Å in the basal plane along $\langle 110\rangle$. As satellites antipodal to (0, 0, 5) arise from the same domain of the incommensurate modulation axis, four crystallographically equivalent domains are distinguished that were populated equally after zero-field cooling. Maxima at reciprocal-space positions with $l<5$ are labeled by an index enumerating the domains. Maxima at $l>5$ attributed to the same domain are denoted by an asterisk. In the $\pi\rightarrow\sigma'$ polarization channel, the maxima at $\boldsymbol{Q}_{\mathrm{cycl},3}$ and $\boldsymbol{Q}_{\mathrm{cycl},4}$ are weak due to well-understood polarization effects for the scattering geometry chosen here, although all domains are populated equally (see Supplemental Material [67]).

The scattering intensity in phase B ($H_1<H<H_2$) is characteristic of domains with an in-plane modulation perpendicular to the field (red spheres). In this field range, satellites at $\boldsymbol{Q}_{\mathrm{cycl},3}$ and $\boldsymbol{Q}_{\mathrm{cycl},4}$ vanish, while the modulation lengths remain unchanged $c/(2\delta_1)\approx 64$ Å along [001] and $a/(2\sqrt{2}\epsilon)\approx 215$ Å in the basal plane along $\langle 110\rangle$. Accordingly, the in-plane modulation remains aligned with the crystallographic axes rather than following the low-symmetry field direction. The domain populations display hysteresis as a function of field, as illustrated in the Supplemental Material [67].

Other than in phases A and B, scattering intensity in phase C ($H_2<H<H_3$) was only observed at (0, 0, 5) (orange sphere), characteristic of single-domain commensurate antiferromagnetic order without superlattice modulations. Entering phase D ($H_3<H<H_4$), weak magnetic intensity at $(0,0,5\pm\delta_2)$ with $\delta_2=0.114(6)$ is observed (yellow spheres), characteristic of single-domain incommensurate order with a modulation length 43 Å of the staggered magnetization along [001] and no superlattice modulation in the basal plane. For fields exceeding the highest critical fields observed in the bulk properties, i.e., $H_4<H$, no scattering intensity was observed as expected of the field-polarized state.

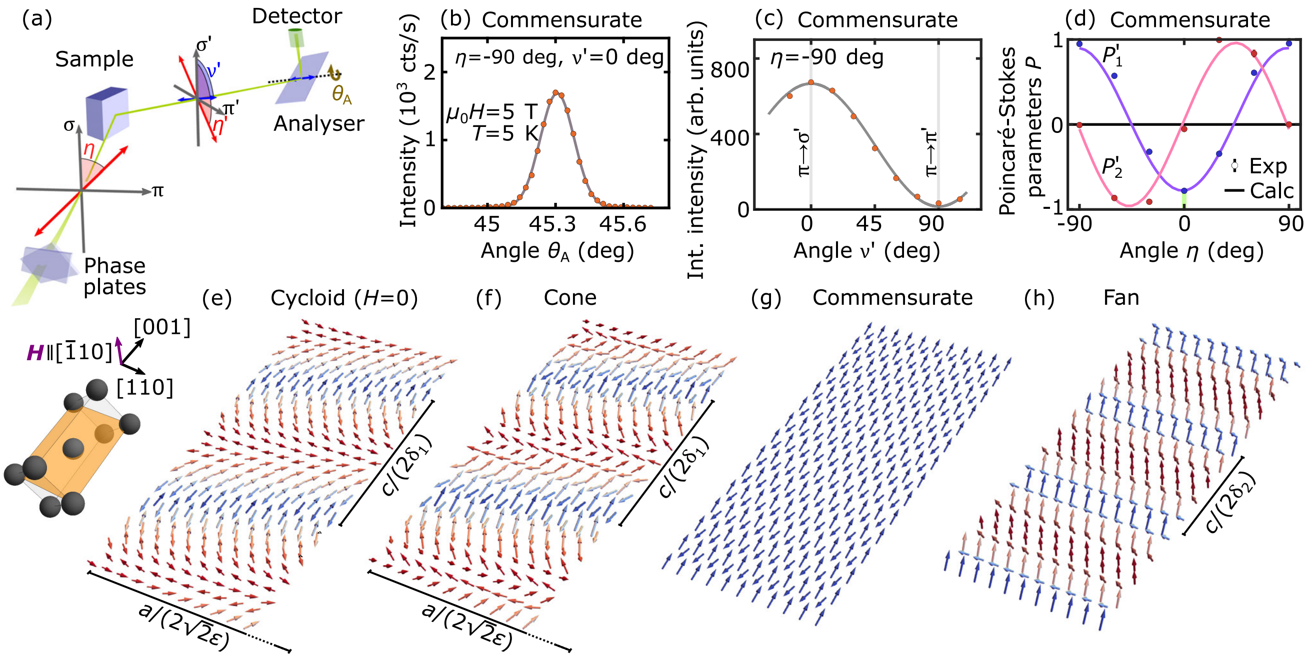

FIG. 3. Magnetic structure refinement by means of FLPA. (a) Schematic depiction of the setup used for FLPA. Variables without and with prime denote quantities before and after scattering. Polarization directions π and σ are in and perpendicular to the scattering plane, respectively. The direction of the x-ray polarization (red double-headed arrow) with respect to σ is denoted by the angle η. The rotatable analyzer crystal selects a polarization direction enclosing an angle ν' with σ'. The crystal may be rocked by the angle Θ_A. Phase plates determine the incident polarization [77]. (b) Rocking scan of the analyzer for a given incident (π) and scattered (σ') polarization channel. Integrated intensity is inferred from a Gaussian fit (solid line). Typical data for the commensurate phase are shown. (c) Integrated intensity for a given incident polarization (π) as a function of the analyzer orientation ν' and Poincaré-Stokes fit (solid line). Magnetic intensity in channels $\pi \to \sigma'$ and $\pi \to \pi'$ reflect magnetization components in and perpendicular to the scattering plane. (d) Poincaré-Stokes parameters P'_1 and P'_2 as a function of the incident polarization angle η. Solid lines correspond to calculations based on commensurate antiferromagnetic order. Discrepancy from $P'_1 = -1$ at $\eta = 0$, marked in green, is attributed to charge scattering. (e)–(h) Schematic real-space depictions of the magnetic structure in the different phases in the crystallographic $(1\bar{1}0)$ plane (orange shading). Blue and red colors indicate large and small components along [001]. The modulation length refers to the staggered magnetization.

To determine the nature of the magnetic order unambiguously, FLPA was carried out in each magnetic phase for magnetic field parallel to $[\bar{1}10]$ [63,64]. The experimental setup is schematically depicted in Fig. 3(a). The procedure is illustrated by means of data recorded in the commensurate phase shown in Figs. 3(b)–3(d), cf. Supplemental Material for data recorded in the other phases [67]. For a given polarization angle η of the incident beam, the scattering intensity for a given orientation of the analyzer crystal ν' was determined by integrating over a rocking scan of the analyzer crystal using a Gaussian fit [78] [Fig. 3(b)]. Such rocking scans were carried out for a series of analyzer orientations ν'. Fitting the integrated intensities with the equation $f(\nu') \propto 1 + P'_1 \cos 2\nu' + P'_2 \sin 2\nu'$ [Fig. 3(c)], the linear polarization of the scattered beam was determined in terms of its Poincaré-Stokes parameters P'_1 and P'_2, cf. Supplemental Material [67]. This measurement protocol was repeated for different values of η [79]. Finally, starting from the irreducible representations, values of the Poincaré-Stokes parameters $P'^{\mathrm{calc}}_1(\eta_i)$ and $P'^{\mathrm{calc}}_2(\eta_i)$ were calculated for each candidate magnetic structure and compared with the seven pairs of Poincaré-Stokes parameters experimentally determined [Fig. 3(d)].

Crucial for the refinement of the magnetic structure, the FLPA allowed us to single out the spin scattering contributions. Namely, in all magnetic phases scattering intensity was also observed under unchanged linear polarization; i.e., special care has to be taken to distinguish magnetic from nonmagnetic scattering contributions. In the $\sigma \to \sigma'$ channel, the scattering must be purely nonmagnetic, while it may be magnetic or nonmagnetic in the $\pi \to \pi'$ channel [76,80]. For the magnetic structure refinement, it was assumed that the nonmagnetic scattering is due to charge scattering. For increasing magnetic field going from phase A to phase D, inclusion of the charge scattering improved the goodness of fit dramatically, cf. Supplemental Material [67]. In addition, intensity maxima were observed in the cycloidal and conical phase in the $\pi \to \pi'$ channel at $(0, 0, 5 \pm \delta_1)$, independent of the magnetic satellites. This intensity may be the characteristic of so-called truncation rods arising from finite penetration depth or a symmetry reduction due to structural modulations or charge-density wave order [27]. While further studies are needed to resolve the origin of the charge scattering, determination of the magnetic structures pursued here turns out to be robust.

The magnetic structures inferred from REXS with FLPA, taking charge scattering into account, are depicted schematically for the crystallographic $(1\bar{1}0)$ plane in Figs. 3(e)–3(h). Starting with phase A, shown in Fig. 3(e), type A antiferromagnetism is observed with an antiparallel coupling of the moments along the $\langle 111 \rangle$ directions and a long-wavelength cycloidal superstructure. The superstructure exhibits modulations along [001] and one of the $\langle 110 \rangle$ axes. This superstructure supports four equivalent domain populations in zero field. Figure 3(e) depicts the domain associated with $\boldsymbol{Q}_{\mathrm{cycl},1}$. Considering phase B, depicted in Fig. 3(f), the same type A antiferromagnetism persists with a superstructure that is closely related to the cycloid, supporting modulations along [001] and perpendicular to the field direction. The main difference with respect to phase A is the uniform magnetization along the field direction. Thus, with increasing field the opening angle of the conical structure decreases.

Phase C, shown in Fig. 3(g), represents commensurate type A antiferromagnetism in which ferromagnetic layers of moments parallel and antiparallel to the [001] axis alternate along the same axis, superimposed with a uniform magnetization along the field direction. The resulting magnetic structure is noncollinear but coplanar without additional twisting or scalar spin chiralities. Finally, as shown in Fig. 3(h), phase D corresponds to type A order with a long-wavelength amplitude-modulated superstructure of moments pointing along [001] and a uniform magnetization along the field direction. This modulation may be referred to as fanlike and differs distinctly from the cycloidal and conical modulations.

Considering the DM vectors permitted by the crystal structure [61], Hamiltonian contributions of magnetic moments for the next-nearest-neighbor bonds along $\langle 111 \rangle$ perpendicular to the field direction $[\bar{1}10]$ favor spin canting around $[\bar{1}10]$, such as in the cycloidal and conical state. For next-nearest-neighbor bonds along $\langle 111 \rangle$ perpendicular to [110], instead spin canting around [110] is favored, as observed in the fanlike phase. In combination with the Zeeman energy in applied fields, modulated states as different as the cycloidal and the fanlike state may be realized.

We finally note that the critical field of the field-polarized state of order 9 T, which sets the scale of the antiferromagnetic exchange interactions, exhibits comparatively small anisotropy [60,61]. As the commensurate phase is encompassed by the phases supporting cycloidal, conical, and fanlike superstructures, the DM spin-orbit coupling must be comparable in strength to the antiferromagnetic exchange. Thus, building on the advantages offered by REXS with FLPA in studies of antiferromagnetic superstructures and materials not amenable to neutron scattering, we identify a highly unusual combination of interactions and magnetic phases which, to the best of our knowledge, has neither been reported experimentally nor addressed theoretically before.

We wish to thank M. Azhar, M. Garst, F. Haslbeck, J. R. Linares Mardegan, S. Mayr, A. Senyshyn, S. Sorn, and M. Wilde for fruitful discussions and assistance with the experiments. This study has been funded by the Deutsche Forschungsgemeinschaft (DFG, German Research Foundation) under TRR80 (From Electronic Correlations to Functionality, Project No. 107745057, Project E1), SPP2137 (Skyrmionics, Project No. 403191981, Grant No. PF393/19), and the excellence cluster MCQST under Germany's Excellence Strategy EXC-2111 (Project No. 390814868). Financial support by the European Research Council (ERC) through Advanced Grants No. 291079 (TOPFIT) and No. 788031 (ExQuiSid) as well as through the European Union's Horizon 2020 research and innovation program under the Marie Skłodowska-Curie Grant Agreement No. 884104 (PSI-FELLOW-III-3i) is gratefully acknowledged. We acknowledge DESY (Hamburg, Germany), a member of the Helmholtz Association HGF, for the provision of experimental facilities. Parts of this research were carried out at beam line P09 at PETRA III at DESY. Beam times were allocated for proposals I-20180440 and I-20200748.

*Corresponding author.
wolfgang.simeth@psi.ch

[1] P. Bak, Commensurate phases, incommensurate phases and the devil's staircase, Rep. Prog. Phys. **45**, 587 (1982).

[2] Y. A. Izyumov, Modulated, or long-periodic, magnetic structures of crystals, Sov. Phys. Usp. **27**, 845 (1984).

[3] H. Z. Cummins, Experimental studies of structurally incommensurate crystal phases, Phys. Rep. **185**, 211 (1990).

[4] N. Nagaosa and Y. Tokura, Topological properties and dynamics of magnetic skyrmions, Nat. Nanotechnol. **8**, 899 (2013).

[5] C. Back, V. Cros, H. Ebert, K. Everschor-Sitte, A. Fert, M. Garst, T. Ma, S. Mankovsky, T. L. Monchesky, M. Mostovoy, N. Nagaosa, S. S. P. Parkin, C. Pfleiderer, N. Reyren, A. Rosch, Y. Taguchi, Y. Tokura, K. von Bergmann, and J. Zang, The 2020 skyrmionics roadmap, J. Phys. D **53**, 363001 (2020).

[6] I. Dzyaloshinsky, A thermodynamic theory of "weak" ferromagnetism of antiferromagnetics, J. Phys. Chem. Solids **4**, 241 (1958).

[7] T. Moriya, Anisotropic superexchange interaction and weak ferromagnetism, Phys. Rev. **120**, 91 (1960).

[8] Y. Ishikawa, K. Tajima, D. Bloch, and M. Roth, Helical spin structure in manganese silicide MnSi, Solid State Commun. **19**, 525 (1976).

[9] K. Motoya, H. Yasuoka, Y. Nakamura, and J. H. Wernick, Helical spin structure in MnSi-NMR studies, Solid State Commun. **19**, 529 (1976).

[10] J. Beille, J. Voiron, F. Towfiq, M. Roth, and Z. Y. Zhang, Helimagnetic structure of the $Fe_{1-x}Co_xSi$ alloys, J. Phys. F **11**, 2153 (1981).

[11] B. Lebech, Magnetic ordering in nearly ferromagnetic antiferromagnetic helices, in *Recent Advances in Magnetism of Transition Metal Compounds*, edited by A. Kotani and N. Suzuki (World Scientific, Singapore, 1993), p. 167.

[12] Y. Togawa, T. Koyama, K. Takayanagi, S. Mori, Y. Kousaka, J. Akimitsu, S. Nishihara, K. Inoue, A. S. Ovchinnikov, and J. Kishine, Chiral Magnetic Soliton Lattice on a Chiral Helimagnet, Phys. Rev. Lett. **108**, 107202 (2012).

[13] S. Mühlbauer, B. Binz, F. Jonietz, C. Pfleiderer, A. Rosch, A. Neubauer, R. Georgii, and P. Böni, Skyrmion lattice in a chiral magnet, Science **323**, 915 (2009).

[14] X. Z. Yu, Y. Onose, N. Kanazawa, J. H. Park, J. H. Han, Y. Matsui, N. Nagaosa, and Y. Tokura, Real-space observation of a two-dimensional skyrmion crystal, Nature (London) **465**, 901 (2010).

[15] N. Kanazawa, J.-H. Kim, D. S. Inosov, J. S. White, N. Egetenmeyer, J. L. Gavilano, S. Ishiwata, Y. Onose, T. Arima, B. Keimer, and Y. Tokura, Possible skyrmion-lattice ground state in the B20 chiral-lattice magnet MnGe as seen via small-angle neutron scattering, Phys. Rev. B **86**, 134425 (2012).

[16] N. Kanazawa, K. Shibata, and Y. Tokura, Variation of spin-orbit coupling and related properties in skyrmionic system $Mn_{1-x}Fe_xGe$, New J. Phys. **18**, 045006 (2016).

[17] A. Bauer and C. Pfleiderer, Generic aspects of skyrmion lattices in chiral magnets, in *Topological Structures in Ferroic Materials: Domain Walls, Vortices and Skyrmions*, edited by J. Seidel (Springer, New York, 2016), p. 1.

[18] A. Bauer, A. Chacon, M. Wagner, M. Halder, R. Georgii, A. Rosch, C. Pfleiderer, and M. Garst, Symmetry breaking, slow relaxation dynamics, and topological defects at the field-induced helix reorientation in MnSi, Phys. Rev. B **95**, 024429 (2017).

[19] A. Chacon, L. Heinen, M. Halder, A. Bauer, W. Simeth, S. Mühlbauer, H. Berger, M. Garst, A. Rosch, and C. Pfleiderer, Observation of two independent skyrmion phases in a chiral magnetic material, Nat. Phys. **14**, 936 (2018).

[20] L. Lundgren, O. Beckman, V. Attia, S. P. Bhattacheriee, and M. Richardson, Helical spin arrangement in cubic FeGe, Phys. Scr. **1**, 69 (1970).

[21] D. Bloch, J. Voiron, V. Jaccarino, and J. H. Wernick, The high field-high pressure magnetic properties of MnSi, Phys. Lett. **51A**, 259 (1975).

[22] A. Bauer, A. Neubauer, C. Franz, W. Münzer, M. Garst, and C. Pfleiderer, Quantum phase transitions in single-crystal $Mn_{1-x}Fe_xSi$ and $Mn_{1-x}Co_xSi$: Crystal growth, magnetization, ac susceptibility, and specific heat, Phys. Rev. B **82**, 064404 (2010).

[23] M. Stavinoha, J. A. Cooley, S. G. Minasian, T. M. McQueen, S. M. Kauzlarich, C.-L. Huang, and E. Morosan, Charge density wave behavior and order-disorder in the antiferromagnetic metallic series $Eu(Ga_{1-x}Al_x)_4$, Phys. Rev. B **97**, 195146 (2018).

[24] T. Shang, Y. Xu, D. J. Gawryluk, J. Z. Ma, T. Shiroka, M. Shi, and E. Pomjakushina, Anomalous Hall resistivity and possible topological Hall effect in the $EuAl_4$ antiferromagnet, Phys. Rev. B **103**, L020405 (2021).

[25] W. R. Meier, J. R. Torres, R. P. Hermann, J. Zhao, B. Lavina, B. C. Sales, and A. F. May, Thermodynamic insights into the intricate magnetic phase diagram of $EuAl_4$, Phys. Rev. B **106**, 094421 (2022).

[26] X. Y. Zhu, H. Zhang, D. J. Gawryluk, Z. X. Zhen, B. C. Yu, S. L. Ju, W. Xie, D. M. Jiang, W. J. Cheng, Y. Xu, M. Shi, E. Pomjakushina, Q. F. Zhan, T. Shiroka, and T. Shang, Spin order and fluctuations in the $EuAl_4$ and $EuGa_4$ topological antiferromagnets: A μSR study, Phys. Rev. B **105**, 014423 (2022).

[27] J. M. Moya, S. Lei, E. M. Clements, C. S. Kengle, S. Sun, K. Allen, Q. Li, Y. Y. Peng, A. A. Husain, M. Mitrano, M. J. Krogstad, R. Osborn, A. B. Puthirath, S. Chi, L. Debeer-Schmitt, J. Gaudet, P. Abbamonte, J. W. Lynn, and E. Morosan, Incommensurate magnetic orders and topological Hall effect in the square-net centrosymmetric $EuGa_2Al_2$ system, Phys. Rev. Mater. **6**, 074201 (2022).

[28] R. Takagi, N. Matsuyama, V. Ukleev, L. Yu, J. S. White, S. Francoual, J. R. L. Mardegan, S. Hayami, H. Saito, K. Kaneko, K. Ohishi, Y. Ōnuki, T.-hisa Arima, Y. Tokura, T. Nakajima, and S. Seki, Square and rhombic lattices of magnetic skyrmions in a centrosymmetric binary compound, Nat. Commun. **13**, 1472 (2022).

[29] N. D. Khanh, T. Nakajima, X. Yu, S. Gao, K. Shibata, M. Hirschberger, Y. Yamasaki, H. Sagayama, H. Nakao, L. Peng, K. Nakajima, R. Takagi, T.-hisa Arima, Y. Tokura, and S. Seki, Nanometric square skyrmion lattice in a centrosymmetric tetragonal magnet, Nat. Nanotechnol. **15**, 444 (2020).

[30] Y. Yasui, C. J. Butler, N. D. Khanh, S. Hayami, T. Nomoto, T. Hanaguri, Y. Motome, R. Arita, T.-hisa Arima, Y. Tokura, and S. Seki, Imaging the coupling between itinerant electrons and localised moments in the centrosymmetric skyrmion magnet $GdRu_2Si_2$, Nat. Commun. **11**, 5925 (2020).

[31] T. Kurumaji, T. Nakajima, M. Hirschberger, A. Kikkawa, Y. Yamasaki, H. Sagayama, H. Nakao, Y. Taguchi, T. Arima, and Y. Tokura, Skyrmion lattice with a giant topological Hall effect in a frustrated triangular-lattice magnet, Science **365**, 914 (2019).

[32] M. Hirschberger, T. Nakajima, S. Gao, L. Peng, A. Kikkawa, T. Kurumaji, M. Kriener, Y. Yamasaki, H. Sagayama, H. Nakao, K. Ohishi, K. Kakurai, Y. Taguchi, X. Yu, T.-hisa Arima, and Y. Tokura, Skyrmion phase and competing magnetic orders on a breathing kagomé lattice, Nat. Commun. **10**, 5831 (2019).

[33] J. Jiang and S. M. Kauzlarich, Colossal magnetoresistance in a rare earth Zintl compound with a new structure type: $EuIn_2P_2$, Chem. Mater. **18**, 435 (2006).

[34] A. M. Goforth, P. Klavins, J. C. Fettinger, and S. M. Kauzlarich, Magnetic properties and negative colossal magnetoresistance of the rare earth Zintl phase $EuIn_2As_2$, Inorg. Chem. **47**, 11048 (2008).

[35] C. D. Cao, R. Klingeler, H. Vinzelberg, N. Leps, W. Löser, G. Behr, F. Muranyi, V. Kataev, and B. Büchner, Magnetic anisotropy and ferromagnetic correlations above the Curie

temperature in Eu_2CuSi_3 single crystals, Phys. Rev. B **82**, 134446 (2010).

[36] P. F. S. Rosa, C. B. R. de Jesus, Z. Fisk, and P. G. Pagliuso, Physical properties of $EuPtIn_4$ intermetallic antiferromagnet, J. Magn. Magn. Mater. **371**, 5 (2014).

[37] N. J. Ghimire, A. S. Botana, J. S. Jiang, J. Zhang, Y.-S. Chen, and J. F. Mitchell, Large anomalous Hall effect in the chiral-lattice antiferromagnet $CoNb_3S_6$, Nat. Commun. **9**, 3280 (2018).

[38] M. C. Rahn, J.-R. Soh, S. Francoual, L. S. I. Veiga, J. Strempfer, J. Mardegan, D. Y. Yan, Y. F. Guo, Y. G. Shi, and A. T. Boothroyd, Coupling of magnetic order and charge transport in the candidate Dirac semimetal $EuCd_2As_2$, Phys. Rev. B **97**, 214422 (2018).

[39] J.-R. Soh, C. Donnerer, K. M. Hughes, E. Schierle, E. Weschke, D. Prabhakaran, and A. T. Boothroyd, Magnetic and electronic structure of the layered rare-earth pnictide $EuCd_2Sb_2$, Phys. Rev. B **98**, 064419 (2018).

[40] K. S. Takahashi, H. Ishizuka, T. Murata, Q. Y. Wang, Y. Tokura, N. Nagaosa, and M. Kawasaki, Anomalous Hall effect derived from multiple Weyl nodes in high-mobility $EuTiO_3$ films, Sci. Adv. **4**, eaar7880 (2018).

[41] T. Asaba, Y. Su, M. Janoschek, J. D. Thompson, S. M. Thomas, E. D. Bauer, S.-Z. Lin, and F. Ronning, Large tunable anomalous Hall effect in the kagome antiferromagnet $U_3Ru_4Al_{12}$, Phys. Rev. B **102**, 035127 (2020).

[42] J. Gaudet, H.-Y. Yang, S. Baidya, B. Lu, G. Xu, Y. Zhao, J. A. Rodriguez-Rivera, C. M. Hoffmann, D. E. Graf, D. H. Torchinsky, P. Nikolić, D. Vanderbilt, F. Tafti, and C. L. Broholm, Weyl-mediated helical magnetism in NdAlSi, Nat. Mater. **20**, 1650 (2021).

[43] Z.-C. Wang, J. D. Rogers, X. Yao, R. Nichols, K. Atay, B. Xu, J. Franklin, I. Sochnikov, P. J. Ryan, D. Haskel, and F. Tafti, Colossal magnetoresistance without mixed valence in a layered phosphide crystal, Adv. Mater. **33**, 2005755 (2021).

[44] S. Seiro and C. Geibel, Complex and strongly anisotropic magnetism in the pure spin system $EuRh_2Si_2$, J. Phys. Condens. Matter **26**, 046002 (2013).

[45] W. T. Jin, N. Qureshi, Z. Bukowski, Y. Xiao, S. Nandi, M. Babij, Z. Fu, Y. Su, and T. Brückel, Spiral magnetic ordering of the Eu moments in $EuNi_2As_2$, Phys. Rev. B **99**, 014425 (2019).

[46] W. Xie, S. S. Luo, H. Su, X. Y. Zheng, Z. Y. Nie, M. Smidman, T. Takabatake, and H. Q. Yuan, Complex magnetic phase diagram in noncentrosymmetric EuPtAs, Phys. Rev. B **104**, 174425 (2021).

[47] N. Kimura, K. Ito, K. Saitoh, Y. Umeda, H. Aoki, and T. Terashima, Pressure-Induced Superconductivity in Noncentrosymmetric Heavy-Fermion $CeRhSi_3$, Phys. Rev. Lett. **95**, 247004 (2005).

[48] I. Sugitani, Y. Okuda, H. Shishido, T. Yamada, A. Thamizhavel, E. Yamamoto, T. D. Matsuda, Y. Haga, T. Takeuchi, R. Settai, and Y. Ōnuki, Pressure-induced heavy-fermion superconductivity in antiferromagnet $CeIrSi_3$ without inversion symmetry, J. Phys. Soc. Jpn. **75**, 043703 (2006).

[49] N. Kumar, P. K. Das, R. Kulkarni, A. Thamizhavel, S. K. Dhar, and P. Bonville, Antiferromagnetic ordering in $EuPtGe_3$, J. Phys. Condens. Matter **24**, 036005 (2012).

[50] D. Kaczorowski, B. Belan, and R. Gladyshevskii, Magnetic and electrical properties of $EuPdGe_3$, Solid State Commun. **152**, 839 (2012).

[51] M. A. Albedah, K. Al-Qadi, Z. M. Stadnik, and J. Przewoźnik, Antiferromagnetism in $EuPdGe_3$, J. Alloy Compd. **613**, 344 (2014).

[52] A. Maurya, P. Bonville, A. Thamizhavel, and S. K. Dhar, $EuNiGe_3$, an anisotropic antiferromagnet, J. Phys. Condens. Matter **26**, 216001 (2014).

[53] O. Bednarchuk and D. Kaczorowski, Low-temperature physical properties of single-crystalline $EuCoGe_3$ and $EuRhGe_3$, Acta Phys. Pol. A **127**, 418 (2015).

[54] O. Bednarchuk and D. Kaczorowski, Strongly anisotropic and complex magnetic behavior in $EuRhGe_3$, J. Alloy Compd. **646**, 291 (2015).

[55] O. Bednarchuk, A. Gagor, and D. Kaczorowski, Synthesis, crystal structure and physical properties of $EuTGe_3$ ($T = $ Co, Ni, Rh, Pd, Ir, Pt) single crystals, J. Alloy Compd. **622**, 432 (2015).

[56] A. Maurya, P. Bonville, R. Kulkarni, A. Thamizhavel, and S. K. Dhar, Magnetic properties and complex magnetic phase diagram in non-centrosymmetric $EuRhGe_3$ and $EuIrGe_3$ single crystals, J. Magn. Magn. Mater. **401**, 823 (2016).

[57] X. Fabrèges, A. Gukasov, P. Bonville, A. Maurya, A. Thamizhavel, and S. K. Dhar, Exploring metamagnetism of single crystalline $EuNiGe_3$ by neutron scattering, Phys. Rev. B **93**, 214414 (2016).

[58] T. Matsumura, M. Tsukagoshi, Y. Ueda, N. Higa, A. Nakao, K. Kaneko, M. Kakihana, M. Hedo, T. Nakama, and Y. Ōnuki, Cycloidal magnetic ordering in enoncentrosymmetric $EuIrGe_3$, J. Phys. Soc. Jpn. **91**, 073703 (2022).

[59] B. K. Rai, P. O'Rourke, and U. N. Roy, Review on crystal structures and magnetic properties of RTX_3 materials, J. Phys. Condens. Matter **34**, 273002 (2022).

[60] N. Kumar, S. K. Dhar, A. Thamizhavel, P. Bonville, and P. Manfrinetti, Magnetic properties of $EuPtSi_3$ single crystals, Phys. Rev. B **81**, 144414 (2010).

[61] A. Bauer, A. Senyshyn, R. Bozhanova, W. Simeth, C. Franz, S. Gottlieb-Schönmeyer, M. Meven, T. E. Schrader, and C. Pfleiderer, Magnetic properties of the noncentrosymmetric tetragonal antiferromagnet $EuPtSi_3$, Phys. Rev. Mater. **6**, 034406 (2022).

[62] A. N. Bogdanov and D. A. Yablonskii, Thermodynamically stable "vortices" in magnetically ordered crystals. The mixed state of magnets, Sov. Phys. JETP **68**, 101 (1989), http://jetp.ras.ru/cgi-bin/e/index/e/68/1/p101?a=list.

[63] C. Mazzoli, S. B. Wilkins, S. Di Matteo, B. Detlefs, C. Detlefs, V. Scagnoli, L. Paolasini, and P. Ghigna, Disentangling multipole resonances through a full x-ray polarization analysis, Phys. Rev. B **76**, 195118 (2007).

[64] P. D. Hatton, R. D. Johnson, S. R. Bland, C. Mazzoli, T. A. W. Beale, C. H. Du, and S. B. Wilkins, Magnetic structure determination using polarised resonant X-ray scattering, J. Magn. Magn. Mater. **321**, 810 (2009).

[65] D. K. Shukla, S. Francoual, A. Skaugen, M. v. Zimmermann, H. C. Walker, L. N. Bezmaternykh, I. A. Gudim, V. L. Temerov, and J. Strempfer, Ho and Fe magnetic ordering in multiferroic $HoFe_3(BO_3)_4$, Phys. Rev. B **86**, 224421 (2012).

[66] S. L. Zhang, A. Bauer, H. Berger, C. Pfleiderer, G. van der Laan, and T. Hesjedal, Resonant elastic x-ray scattering from the skyrmion lattice in Cu_2OSeO_3, Phys. Rev. B **93**, 214420 (2016).

[67] See Supplemental Material at http://link.aps.org/supplemental/10.1103/PhysRevLett.130.266701 for a description of the experimental methods and detailed account of the full linear polarization analysis, which includes Refs. [68–73].

[68] A. Neubauer, J. Bœuf, A. Bauer, B. Russ, H. v. Löhneysen, and C. Pfleiderer, Ultra-high vacuum compatible image furnace, Rev. Sci. Instrum. **82**, 013902 (2011).

[69] U. Fano, Description of states in quantum mechanics by density matrix and operator techniques, Rev. Mod. Phys. **29**, 74 (1957).

[70] G. van der Laan, Soft X-ray resonant magnetic scattering of magnetic nanostructures, C. R. Phys. **9**, 570 (2008).

[71] D. B. Pengra, N. Thoft, M. Wulff, R. Feidenhans'l, and J. Bohr, Resonance-enhanced magnetic X-ray diffraction from a rare-earth alloy, J. Phys. Condens. Matter **6**, 2409 (1994).

[72] R. D. Johnson, S. R. Bland, C. Mazzoli, T. A. W. Beale, C.-H. Du, C. Detlefs, S. B. Wilkins, and P. D. Hatton, Determination of magnetic order of the rare-earth ions in multiferroic $TbMn_2O_5$, Phys. Rev. B **78**, 104407 (2008).

[73] A. S. Wills, A new protocol for the determination of magnetic structures using simulated annealing and representational analysis (SARAh), Physica (Amsterdam) **276-278B**, 680 (2000).

[74] A. Bauer, G. Benka, A. Regnat, C. Franz, and C. Pfleiderer, Ultra-high vacuum compatible preparation chain for intermetallic compounds, Rev. Sci. Instrum. **87**, 113902 (2016).

[75] J. Strempfer, S. Francoual, D. Reuther, D. K. Shukla, A. Skaugen, H. Schulte-Schrepping, T. Kracht, and H. Franz, Resonant scattering and diffraction beamline P09 at PETRA III, J. Synchrotron Radiat. **20**, 541 (2013).

[76] J. P. Hill and D. F. McMorrow, Resonant exchange scattering: Polarization dependence and correlation function, Acta Crystallogr. Sect. A **52**, 236 (1996).

[77] S. Francoual, J. Strempfer, D. Reuther, D. K. Shukla, and A. Skaugen, Double phase-retarder set-up at beamline P09 at PETRA III, J. Phys. Conf. Ser. **425**, 132010 (2013).

[78] C. Detlefs, Polarization analysis of K-edge resonant X-ray scattering of Germanium, Physica (Amsterdam) **345B**, 45 (2004).

[79] C. Detlefs, M. Sanchez del Rio, and C. Mazzoli, X-ray polarization: General formalism and polarization analysis, Eur. Phys. J. Special Topics **208**, 359 (2012).

[80] M. Blume and D. Gibbs, Polarization dependence of magnetic x-ray scattering, Phys. Rev. B **37**, 1779 (1988).